Hydrogen-impurity-induced unconventional magnetism in semiconducting molybdenum ditelluride

Jonas A. Krieger,[1,2,3,*] Daniel Tay,[3] Igor P. Rusinov,[4,5] Sourabh Barua,[6,†] Pabitra K. Biswas,[7] Lukas Korosec,[3] Thomas Prokscha,[1] Thorsten Schmitt,[2] Niels B. M. Schröter,[2,*] Tian Shang,[8,‡] Toni Shiroka,[1,3] Andreas Suter,[1] Geetha Balakrishnan,[6] Evgueni V. Chulkov,[4,5,9,10] Vladimir N. Strocov,[2,§] and Zaher Salman[1,‖]

[1]*Laboratory for Muon Spin Spectroscopy, Paul Scherrer Institute, CH-5232 Villigen PSI, Switzerland*
[2]*Swiss Light Source, Paul Scherrer Institute, CH-5232 Villigen PSI, Switzerland*
[3]*Laboratorium für Festkörperphysik, ETH Zürich, CH-8093 Zürich, Switzerland*
[4]*Tomsk State University, pr. Lenina 36, 634050 Tomsk, Russia*
[5]*St. Petersburg State University, Universitetskaya nab. 7/9, 199034 St. Petersburg, Russia*
[6]*Department of Physics, University of Warwick, Coventry CV4 7AL, United Kingdom*
[7]*ISIS Facility, Rutherford Appleton Laboratory, Chilton, Didcot, Oxon OX110QX, United Kingdom*
[8]*Laboratory for Multiscale Materials Experiments, Paul Scherrer Institut, CH-5232 Villigen PSI, Switzerland*
[9]*Donostia International Physics Center, P. Manuel de Lardizabal 4, San Sebastián, 20018 Basque Country, Spain*
[10]*Departamento de Polímeros y Materiales Avanzados: Física, Química y Tecnología, Facultad de Ciencias Químicas, Aptdo. 1072, 20018 San Sebastián, Spain*

(Received 30 May 2022; revised 24 February 2023; accepted 5 April 2023; published 28 April 2023)

Layered transition-metal dichalcogenides are proposed as building blocks for van der Waals heterostructures due to their graphenelike two-dimensional structure. For this purpose, a magnetic semiconductor could represent an invaluable component for various spintronics and topotronics devices. Here, we combine different local magnetic probe spectroscopies with angle-resolved photoemission and density-functional theory calculations to show that 2*H*-$MoTe_2$ is on the verge of becoming magnetic. Our results present clear evidence that the magnetism can be "switched on" by a hydrogenlike impurity. We also show that this magnetic state survives up to the free surface region, demonstrating the material's potential applicability as a magnetic component for thin-film heterostructures.

DOI: 10.1103/PhysRevMaterials.7.044414

I. INTRODUCTION

Layered transition-metal dichalcogenides (TMDs) are a promising class of materials featuring interesting optoelectronic, superconducting, catalytic, and topological properties. They can also be exfoliated down to monolayers, making them suitable for potential applications in complex van der Waals (vdW) heterostructures [1,2]. Among the TMDs, polymorphic $MoTe_2$ exhibits a variety of electronic and magnetic properties: its metallic 1*T*' phase turns into a T_d phase at ≈250 K [3]. The latter is a topological Weyl semimetal that features unconventional superconductivity at low temperature [4–6]. The 2*H* phase, the most stable one at ambient conditions, is an indirect band gap semiconductor and has been successfully integrated in transistors and photodetectors [7–9]. Moreover, it has been demonstrated that the 2*H* phase can be distorted into the 1*T*′ phase as a function of strain or gate voltage [10,11]. In addition, room temperature (RT) magnetic hysteresis has been observed for small amounts of vanadium deposited on 2*H*-$MoTe_2$ [12]. Most interestingly, 2*H*-$MoTe_2$ was shown by muon spin spectroscopy (μ^+SR) to be a magnetic semiconductor, exhibiting a long-range magnetic order in the bulk at low temperatures, which was tentatively attributed to Mo antisite defects [13]. However, no other technique has reported such long range magnetic order and the origin of this magnetism remains unclear. In fact, theoretical calculations also predict that, apart from antisite defects, hydrogen and transition-metal dopants are able to induce spin polarization in $MoTe_2$ in the monolayer limit [14,15]. A muon can be considered to be an implanted light hydrogen isotope, which can affect its immediate environment and thereby its magnetic response [16–18]. So one possible explanation is that the magnetism observed in μ^+SR is not intrinsic, but rather induced by the muon itself. Another important consideration is that in order to exploit these magnetic properties, e.g., in thin-film

*Current address: Max Planck Institut für Mikrostrukturphysik, Weinberg 2, 06120 Halle, Germany.
†Current address: Department of Physics, Central University of Punjab, Bathinda 151401, India.
‡Current address: Key Laboratory of Polar Materials and Devices (MOE), School of Physics and Electronic Science, East China Normal University, Shanghai 200241, China.
§vladimir.strocov@psi.ch
‖zaher.salman@psi.ch

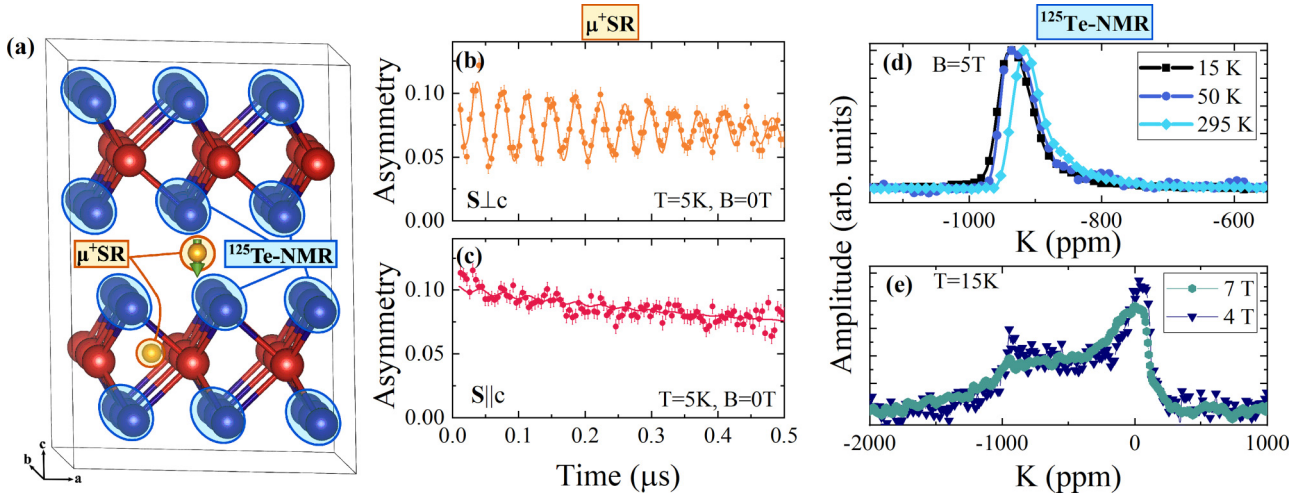

FIG. 1. (a) Schematic illustration of the different probing sites. The muon's stopping sites are interstitial, inside the layer and in the vdW gap, whereas ^{125}Te-NMR is sensitive to the local magnetism at the Te site. The μ^+SR asymmetry spectra measured in zero field at $T = 5.5$ K with the initial muon spin polarization (b) perpendicular ($\perp$) and (c) parallel ($\parallel$) to the c axis of the crystal. Coherent zero-field precession is observed only in (b), indicating that the muons probe a magnetic field along the c axis. (d) ^{125}Te-NMR spectral line shapes of a 2H-$MoTe_2$ single crystal in a field of 5.01 T perpendicular to the c axis at different temperatures. (e) ^{125}Te-NMR powder line shapes at 15 K at different applied fields. The lack of a pronounced temperature or field dependence in the ^{125}Te-NMR lines implies the absence of an intrinsic magnetic order.

heterostructures, one should first elucidate their origin and evolution as a function of depth in the vicinity of an interface (with vacuum or other materials).

Here, we address these questions by utilizing complementary local spin probe measurements, i.e., with implanted muons and with the host's ^{125}Te-NMR, to reveal the origin of the reported magnetism. We find that some of the implanted muons, which form a hydrogenlike state in 2H-$MoTe_2$, detect magnetism in this material. In contrast, ^{125}Te-NMR shows no evidence of any intrinsic magnetic order. These findings were then confirmed by detailed density-functional theory (DFT) calculations, which also reproduce the experimental 3D electronic band structure. When including isolated hydrogen (i.e., muonlike) impurities, the DFT unveils an induced magnetic moment at the impurity. Furthermore, we show that this hydrogen-induced magnetic state remains unchanged towards the crystal surface, establishing 2H-$MoTe_2$ as a switchable magnetic semiconductor by hydrogen doping, thus paving the path towards new possibilities for integrating this intriguing TMD into future applications in thin-film heterostructures.

II. EXPERIMENT

In order to gain a better understanding of the nature of the previously observed magnetic signal in 2H-$MoTe_2$, we combine different local magnetic spectroscopies: (i) μ^+SR which uses individually implanted, spin-polarized muons, stopping at interstitial sites in the lattice, and (ii) NMR on the tellurium nuclei (^{125}Te), intrinsic to the host compound. This is illustrated in Fig. 1(a). Both the muon and the ^{125}Te nuclei have a spin of 1/2 and are, therefore, unaffected by quadrupolar interactions and thus act as purely magnetic probes of the system.

High-quality single crystals of 2H-$MoTe_2$ were grown by the chemical vapor transport method. Stoichiometric amounts of the starting materials, Mo and Te, along with the transport agent $TeCl_4$ (3 mg/cm^3), were mixed together in a quartz ampule and sealed in vacuum. The quartz tube was then placed for 3 weeks in a two-zone horizontal tube furnace with the charge end at 800 °C and the end where the crystals form at 750 °C. Additional characterization measurements confirming the high quality of the single crystals are presented in the Supplemental Material [19]. These include the x-ray diffraction (XRD) and x-ray photoelectron spectroscopy (XPS), in Fig. S1, and the magnetometry measurements with a Quantum Design superconducting quantum interference device (SQUID) magnetic properties measurement system (MPMS) shown in Fig. S2. In order to check the exact stoichiometry/composition of our crystals, we performed an elemental analysis through energy dispersive x-ray spectroscopy (on a scanning electron microscope) on the as-grown single crystals of 2H-$MoTe_2$. Typical results of the stoichiometry obtained by this technique are listed in Table S1, with the results showing the stoichiometry to be as expected (within error) with no islands of excess Te on the surfaces or inclusions of Te in the crystals.

The μ^+SR experiments were performed on the low energy muon [20,21] (LEM) and general purpose spectrometers [22] (GPS) at the Swiss Muon Source, Paul Scherrer Institute, Switzerland. At GPS, the temperature was controlled using a ^{4}He flow cryostat. In order to vary the orientation of the sample with respect to the initial muon spin direction, the sample was mounted on a mechanical rotation stage. Nearly 100 % spin polarized muons were implanted. The asymmetric emission of the muon's decay positrons (lifetime $\tau_\mu = 2.2$ μs) enables us to use them as a local magnetic probe [23]. Note that, at any given moment, there is only one muon in the sample. Therefore, we can exclude that a muon probes magnetism induced by a nearby μ^+ or muonium (Mu), i.e., the hydrogenlike bound state between a muon and an electron.

Oscillation frequencies were extracted by fitting the spectra to a sum of Gaussian damped oscillating components plus a nonoscillating Gaussian damped contribution, using the MUSRFIT software suite [24].

The ^{125}Te-NMR signals were collected by means of spin-echo detection in a $\pi/2$–π sequence, using a 62.5 MHz to 125 MHz duplexer, with a 63 dB preamplifier. The line shapes were then extracted via a fast Fourier transformation of those signals. Typical pulse widths of 5 μs and repetition times of 20 s were used, with each line shape corresponding to more than 20 000 records. Measurements on a single crystal were performed in a field of 5.01 T perpendicular to the c axis, while those on powders were performed in fields of 7.067 T and 4.011 T. The sheetlike single crystal was cut into tagliatellelike strips in order to better fill the NMR measurement tube, possibly leading to a small amount of rotational disorder. The ^{125}Te reference frequencies were calibrated using ^{27}Al-NMR on aluminum foil, which is known to have a very small shift as a function of temperature [25].

Soft x-ray angle-resolved photoemission spectroscopy (ARPES) experiments were performed on the X03MA beamline at the Swiss Light Source of the Paul Scherrer Institute, Villigen, Switzerland [26,27]. The analyzer slit was oriented along the incoming beam direction and the photon energy $h\nu$ was tuned in the range of 320 eV to 900 eV. The high photon energies allow a better k_z resolution [28] than in previous investigations of 2H-$MoTe_2$ [29]. The combined beamline and analyzer resolution was better than 0.15 eV at $h\nu = 900$ eV and better than 63 meV around $h\nu \sim 500$ eV. The samples were cleaved *in situ* and kept at ∼12 K in a vacuum lower than 10^{-10} mbar. We only present the binding energy with respect to the valence band maximum because 2H-$MoTe_2$ tends to statically charge upon x-ray illumination, which causes a rigid shift of the spectrum, as shown by a control measurement of the energy shift as a function of photon flux shown in Fig. S3.

Calculations

The electronic structure was calculated with density-functional theory (DFT) and the projected augmented wave (PAW) method from the VASP code [30,31]. The Hamiltonian contained the scalar relativistic corrections and the spin-orbit coupling was taken into account. The structure was relaxed and the exchange-correlation functional was chosen to be Perdew-Burke-Ernzerhof (PBE) [32]. The parameter for the relaxed cell used in the ARPES calculation were given by $a = 3.491$ Å and $c = 13.647$ Å, where the Mo and Te sit at the $2c$ and $4f$ Wyckoff positions of space group 194, respectively, with relative z coordinates 0.116 and 0.383 for Te. Along Γ-M an orbital decomposition into symmetric $(p_z, p_y, d_{z^2}, d_{x^2-y^2}, d_{zy})$ and antisymmetric (p_x, d_{xy}, d_{xz}) orbitals was performed. The orbital character does not fully separate into symmetric and antisymmetric bands because of spin-orbit coupling. Nevertheless, when using p- (s-) polarized light [Figs. 2(a) and 2(b)], only the symmetric (antisymmetric) part of the electronic wave function, which primarily consists of these orbitals, will be probed.

In order to simulate a single muon impurity, we used a hydrogen pseudopotential in the relaxed $3 \times 3 \times 1$ supercell of 2H-$MoTe_2$. The assumed lattice constants in the $3 \times 3 \times 1$ supercell, $c = 13.647$ Å and a corresponding $a = 10.4745$ Å, were the same as for the band structure calculations. The charge state of the muon is accounted for by assuming a neutral/charged supercell [33,34]. Therein, we performed nudged elastic band (NEB) [35] as well as density of states calculations on the basis of the linear combination of pseudo atomic orbitals (LCPAO) approach as implemented in the OPENMX code [36]. The muon ground state energies were estimated by approximating the NEB diffusion energy barriers with an anisotropic harmonic oscillator potential. The crystal structures were visualized with VESTA [37]. Some further details regarding the stable muon positions are listed in Table S2.

III. RESULTS

The 2H-$MoTe_2$ single crystals used in this study were grown by the chemical vapor transport technique, using $TeCl_4$ as the transporting agent. In contrast, the previously studied samples from Ref. [13] were prepared using Te flux. Therefore, we expect the density and nature of native defects in our samples to be different. This subtle difference should affect their magnetic properties, if long-range magnetism were induced by structural defects. Indeed we observe a coherent precession of the muon spin in zero magnetic field and at low temperature; see Fig. 1(b). However, our μ$^+$SR measurements show identical results to those published earlier, namely yielding the same transition temperature and the same internal magnetic field magnitude. The precession frequency at 5.5 K in Fig. 1(b) corresponds to an internal magnetic field of 199.1(3) mT, consistent with the previously reported value of $\mu_0 H_{\text{int}} = 200$ mT [13]. Additional measurements as a function of temperature and using low-energy muons stopping within 10 nm to 100 nm from the surface are presented in Supplemental Fig. S7 and show a similar behavior [19]. Therefore, we conclude that the local magnetic properties observed with μ$^+$SR in 2H-$MoTe_2$ are robust and do not change in the near-surface region of the crystals, nor do they depend on the details of the sample synthesis. This is an indication that the previously reported structural defects [13] are unlikely to be the origin of long-range magnetic order.

Furthermore, measurements as a function of the angle between the c axis and initial muon spin polarization, as shown in Figs. 1(b) and 1(c), reveal that the internal magnetic field sensed by the muon is oriented along the c axis. A maximal Larmor precession amplitude is detected when the initial muon spin $\mathbf{S} \perp c$ axis [Fig. 1(b)], while it almost vanishes for $\mathbf{S} \parallel c$ axis [Fig. 1(c)]. This implies that the local magnetic field sensed by the implanted muons points along the crystallographic c axis. A detailed analysis of the full angular dependence between the initial muon spin and the c axis is presented in Supplemental Fig. S6 and supports this conclusion.

Contrary to the μ$^+$SR results, we find no signatures of intrinsic magnetism with the ^{125}Te-NMR measurements. Example spectra on several, oriented 2H-$MoTe_2$ single crystals in a field of ≈5.01 T are shown in Fig. 1(d). The spectra neither exhibit a significant broadening nor a resonance shift as a function of temperature, which is strong evidence that the ^{125}Te nuclear spins experience no significant changes in

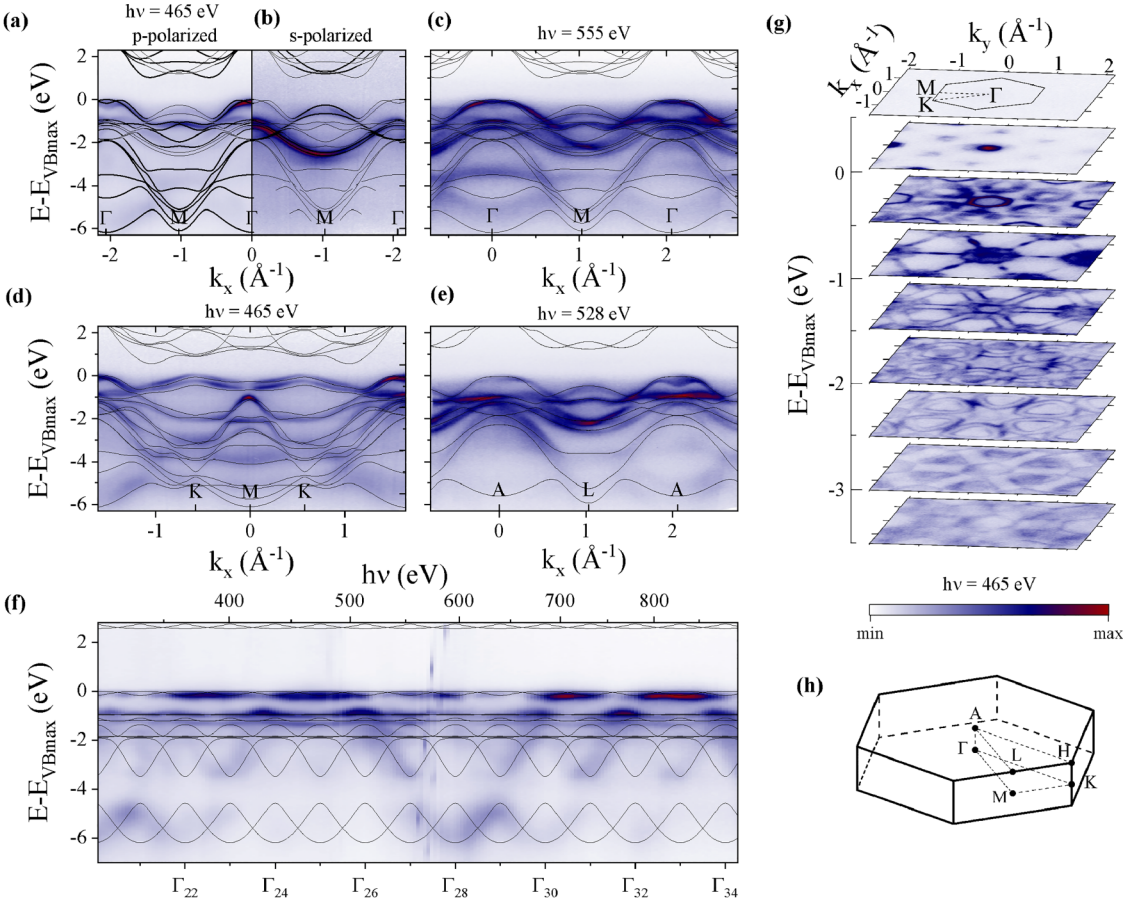

FIG. 2. Comparison of soft x-ray ARPES spectra at ∼12 K with the calculated band structure (solid lines). (a),(b) Dispersion along Γ-*M* at Γ_{25}, (c) along Γ-*M* at Γ_{27}, (d) along *K*-*M* at Γ_{25}, (e) along *A*-*L* between Γ_{26} and Γ_{27}, and (f) along Γ-*A*. (g) Constant energy cuts at Γ_{25}. In (a) and (b) symmetric and antisymmetric bands were probed by using *p*- and *s*-polarized light, respectively. There, the width of the calculated lines represents the contribution of symmetric or antisymmetric orbitals to the band structure. All other spectra were probed with circularly polarized light, which does not distinguish between symmetric and antisymmetric states. (h) Brillouin zone and high symmetry points of 2*H*-$MoTe_2$.

the local spin susceptibility. This is in stark contrast to the typical NMR hallmarks of magnetic ordering, which consist of a temperature-dependent NMR line shift and broadening, caused by the emergence of an internal magnetic field near the magnetic transition, as observed for example in unenriched Fe [38] or in the RAlGe material family [39]. Similar distinctive NMR magnetic signatures are also expected for defect-induced magnetism, as has been observed, e.g., in the 2D system SiC [40].

We exclude the presence of a static magnetic field at the ^{125}Te site by measuring powder line shapes at 15 K in different applied fields; see Fig. 1(e). These spectra are significantly broader than those of single crystals, a broadening which we attribute to an anisotropic chemical shift. However, apart from a small change in the line shape, the linewidth scales perfectly with the applied field. This lack of field dependence is indicative of the nonmagnetic origin of the line broadening, as it excludes the presence of a static internal magnetic field at the ^{125}Te site. Therefore, these results clearly show that an intrinsic spin probe exhibits no evidence of any long-range magnetic order in 2*H*-$MoTe_2$. This is in clear contrast to our observation with μ^+SR and cannot be a consequence of the different timescales probed by μ^+SR and ^{125}Te-NMR, as discussed in the Supplemental Material [19]. We note that the single oscillation frequency observed in μ^+SR implies that any potential magnetic ordering would have to be of fairly high symmetry. In order to exclude that the Te 4*f* site is magnetically compensated, we have considered magnetic subgroups of space group 194 with propagation vectors $\mathbf{k} = (0, 0, 0)$, $\mathbf{k} = (1/2, 0, 0)$, $\mathbf{k} = (0, 0, 1/2)$, and $\mathbf{k} = (1/2, 1/2, 0)$, with a magnetic moment located on the Mo 2*c* site. In none of these subgroups does the field cancel at the Te 4*f* site due to symmetry [41]. Therefore, this is a strong indication that the local static fields observed with muons originate from a muon-induced effect.

In order to reveal the origin of this effect, we use DFT to calculate the ground state of 2*H*-$MoTe_2$ and how it is affected by an individual implanted muon. We start by refining our DFT calculation to reproduce the electronic structure of 2*H*-$MoTe_2$. For this purpose, we determine the three-dimensional electronic band dispersion with soft x-ray ARPES. Spectra along high symmetry directions at photon energies corresponding to the Γ and *A* planes are shown in Figs. 2(a)–2(e). These reveal sharp bands over the whole range of binding energies. We find that the valence band maximum is formed at the Γ point by a band derived from states that are symmetric

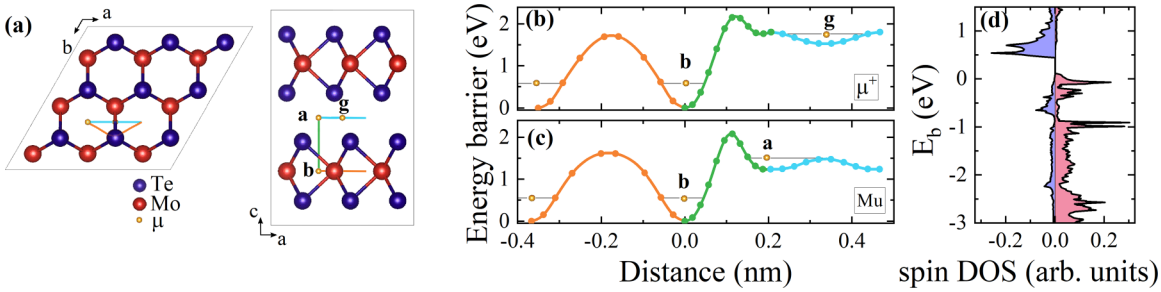

FIG. 3. (a) Stopping sites and diffusion paths indicated in the 3 × 3 × 1 supercell. The muon (μ^+) at sites **b** and **g** and muonium (Mu) at sites **b** and **a**. Energy barrier for (b) μ^+ and (c) Mu diffusion along the different paths. The black lines show the ground-state energy level of the particles at the local minima. (d) Calculated local spin density of states for a muon stopping at site **a**, assuming a nonzero Hubbard U.

along Γ-M. In addition, we measure the band dispersions in k_z along Γ-A as a function of photon energy [Fig. 2(f)]. Along this direction we expect that a two dimensional state forms a flat band with no clear dispersion. In contrast, the dispersive spectral weight in Fig. 2(f) reveals that most bands hybridize across the vdW gap and gain a strong 3D character, despite the 2D layered structure of 2H-$MoTe_2$. Interestingly, the spectral weight exhibits modulations with longer periodicity in k_z than the period of the reciprocal lattice. Such an effect has been previously observed in other 2H-TMDs and is connected with the nonsymmorphic symmetry group of the 2H structure of $MoTe_2$ [42].

We compare the spectral weight in Fig. 2 to the calculated band structure. Note that, in general, *ab initio* DFT calculations of vdW materials can be subject to vdW, spin-orbit, on-site-correlation, and other corrections. Hence they may be misleading unless carefully tuned to the system under investigation. For example, in T_d-$MoTe_2$ an on-site correlation term U(Mo-4d) had to be introduced, to correctly reproduce the experimental results [6,43,44]. However, our DFT calculations, performed without a U(Mo-4d) term, are in excellent agreement with the experimental bands. This indicates that, unlike T_d-$MoTe_2$, in 2H-$MoTe_2$ there are only weak correlations. We further note that there are no signatures of intrinsic magnetism in the calculations of bulk 2H-$MoTe_2$.

By correctly reproducing the 3D band dispersions, we have identified a reliable representation of 2H-$MoTe_2$'s electronic structure and charge density within DFT. We can now employ it to predict the behavior of implanted μ^+ spin probes, introduced as isolated impurities at interstitial positions within a supercell. We consider two charge states of the muon by adding a charge on the supercell (+1 for a diamagnetic μ^+ and +0 for a neutral muon state) [33,34]. The electrically neutral state of a muon corresponds to a muonium. Figure 3 shows the resulting stable stopping sites and the diffusion energy barrier along the most energetically favorable paths between them. In particular, we find that the diamagnetic μ^+ has a stable site **b** (denoted by its Wyckoff letter) inside the Mo layer and a metastable site **g** in the vdW gap. On the other hand, the neutral muonium state can be stable in **b** or metastable in **a**. At the metastable sites the ground-state energy is slightly smaller than the diffusion energy barriers, so we expect muons at these sites to be localized at sufficiently low temperature and to diffuse within the vdW gap at elevated temperatures.

Finally, we consider Mu- and muon-induced magnetism in these sites. Indeed, for the Mu at the site **a**, and when employing a finite Hubbard term U(H-1s) on the hydrogen (i.e., Mu) potential, a significant spin density is induced in the material, Fig. 3(d), while all other sites remain nonmagnetic (Supplemental Fig. S5) [19]. Such muon-induced magnetism is very similar to what was found for hydrogen adsorbed on a monolayer of 2H-$MoTe_2$ or on graphene [14,45].

IV. DISCUSSION

To assess the spectroscopic response of such a state, we consider the hyperfine coupled muonium Hamiltonian $\mathcal{H} = \hbar\mathbf{I}_\mu A\mathbf{S}_e + \hbar\gamma_e\mathbf{S}_e\cdot\mathbf{B}_{\rm ext} + \hbar\gamma_\mu\mathbf{I}_\mu\cdot\mathbf{B}_{\rm ext}$, where A is the hyperfine coupling tensor, $\mathbf{I}_\mu$, and $\mathbf{S}_e$ are the spins of the muon and the bound electron, $\mathbf{B}_{\rm ext}$ denotes the applied field, and $\gamma_e = 2\pi \times 28\,{\rm GHz}/T$ is the electron's gyromagnetic ratio. In the case of the proposed muonium induced magnetism, we can assume that the electron spin $\mathbf{S}_e$ is locked along its local easy axis and remains unaffected by the (relatively small) applied fields. Then the above muonium Hamiltonian can be simplified to

$$\mathcal{H} = \hbar\mathbf{I}_\mu A\mathbf{S}_e + \hbar\gamma_\mu\mathbf{I}_\mu\cdot\mathbf{B}_{\rm ext} = \hbar\gamma_\mu\mathbf{I}_\mu\cdot(\mathbf{B}_{\rm loc}+\mathbf{B}_{\rm ext}), \quad (1)$$

where $A\mathbf{S}_e/\gamma_\mu =: \mathbf{B}_{\rm loc}$ is an effective local magnetic field characterizing the zero field (ZF) oscillation. Therefore, a magnetic muonium would behave identically to a diamagnetic muon in the presence of a local magnetic field. On the other hand, a muonium without locally induced magnetism exhibits four different oscillation frequencies, which scale nonlinearly as a function of field; see, e.g., Refs. [23,46,47]. In the simplified case where $\mathbf{B}_{\rm ext}$ is along the z direction and the hyperfine coupling tensor is aligned to the measurement frame $A = {\rm diag}(\omega_x, \omega_y, \omega_z)$ the corresponding energy levels are

$$E_1/\hbar = \omega_z/4 + \sqrt{\omega_-^2 + (\omega_x-\omega_y)^2/16}, \quad (2)$$

$$E_2/\hbar = -\omega_z/4 + \sqrt{\omega_+^2 + (\omega_x+\omega_y)^2/16}, \quad (3)$$

$$E_4/\hbar = -\omega_z/4 - \sqrt{\omega_+^2 + (\omega_x+\omega_y)^2/16}, \quad (4)$$

$$E_3/\hbar = \omega_z/4 - \sqrt{\omega_-^2 + (\omega_x-\omega_y)^2/16}, \quad (5)$$

where $\omega_\pm = (\gamma_e \pm \gamma_\mu)B_{\rm ext}/2$; cf. Ref. [48]. The μ^+SR oscillation frequencies $\omega_{ij} = (E_i - E_j)/\hbar$ then correspond to transitions between these levels. We note that in the high field limit ($\omega_\pm \gg \omega_x, \omega_y$) the oscillation frequencies mimic

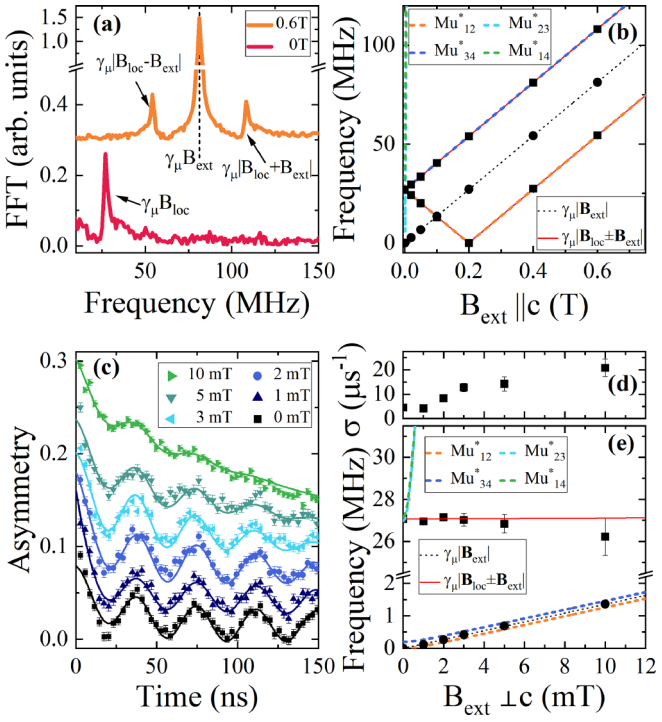

FIG. 4. (a) Fourier transform of the μ^+SR asymmetry spectra measured in ZF and with 0.6 T along c. (b) Corresponding evolution of the oscillation frequencies as a function of the applied field. (c) Asymmetry spectra in a magnetic field applied perpendicular to c with (d) the corresponding damping of the ∼200 mT oscillating component and (e) the oscillation frequencies as a function of applied field. In (b),(e) the solid red line shows the behavior of a muon in a local magnetic field and the dashed lines indicate the behavior of an anisotropic muonium with $A_\parallel$ given by the ZF oscillation frequency with the assumption $A_\perp = 0.2$ MHz. The spectra in (a),(c) have been arbitrarily offset for clarity.

an internal magnetic field along the applied field direction $\omega_{\substack{12\\34}} = \omega_z/2 \mp \gamma_\mu B_{ext}$ determined by the hyperfine coupling along the field direction.

The experimental transverse field dependence of the μ^+SR signal is shown in Fig. 4. As expected, for an external field applied along the c axis, we find that the single ZF peak at $B_{loc} \sim 200$ mT splits up into peaks at $\gamma_\mu|B_{loc} \pm B_{ext}|$, as seen in the fast Fourier transforms of the μ^+SR time spectra in Fig. 4(a). There is an additional component in the spectra, which oscillates at a frequency corresponding to B_{ext} and provides an accurate *in situ* calibration. This component is partially attributed to a background contribution from a silver plate onto which the sample was mounted. Other contributions to this component could also include some diamagnetic muons, which experience no strong magnetic field in 2*H*-$MoTe_2$. The observed behavior in a field along c can be attributed to either (i) an (effective) local magnetic field from a magnetic muonium state or (ii) a very anisotropic muonium state where $A_\parallel \approx 54$ MHz along c and $A_\perp \lesssim 3$ MHz, shown as solid (i) and dashed (ii) lines in Fig. 4(b), respectively. Note that in the latter case we can exclude larger values of $A_\perp$ because they would result in a resolvable splitting of the ZF peak.

We can distinguish between these two scenarios if the transverse field is applied perpendicular to the c axis, Figs. 4(c)–4(e). For a magnetic muonium with an effective local magnetic field, the oscillation frequency should be $\gamma_\mu\sqrt{B_{loc}^2 + B_{ext}^2}$, whereas, for an anisotropic muonium in the high field limit, we expect the appearance of peaks overlapping with the B_{ext} peak. Experimentally, we find that the oscillating component corresponding to $B_{loc} \sim 200$ mT is present up to at least 10 mT, but becomes strongly damped in higher fields, Fig. 4(c). As shown in Fig. 4(e), this is consistent with scenario (i), i.e., the magnetic muonium state described by Eq. (1), and rules out the anisotropic muonium scenario (ii) since that would result in a significant frequency shift in a small applied field. Note that the increase in the damping rate in Fig. 4(d) might be attributed to a small misalignment of the sample's c axis and/or some rotational disorder of structural domains within the sample. Therefore, we conclude that the 2*H*-$MoTe_2$ magnetic response observed with μ^+SR originates from a magnetic muonium state in site **a**. As the muon can be considered a light hydrogen isotope, this induced magnetic state should be the same for a hydrogen atom located at site **a**.

V. CONCLUSIONS

By combining experimental local magnetic probe measurements with ARPES and theoretical DFT calculations, we are able to reveal that 2*H*-$MoTe_2$ is a semiconductor on the verge of becoming magnetic. The comparison of the intrinsic ^{125}Te-NMR probe with the implanted muon spin probe confirms that the observed local field in μ^+SR does not reflect an intrinsic long-range magnetic order. Instead, we find that the muonium, being a hydrogenlike isolated impurity, induces a local magnetic moment in this system.

Importantly, we find that the effect of muonium on the local magnetic properties remains unchanged up to the surface of the crystals. This paves the path towards the use of hydrogen impurities to transform 2*H*-$MoTe_2$ into a magnetic semiconductor building block for vdW heterostructures. We expect that the use of such a material is not limited to applications in spintronics devices [49] but may also include, e.g., Majorana heterostructures [50] or introduction of magnetic proximity at the surface of topological materials [51].

ACKNOWLEDGMENTS

This work is partially based on experiments performed at the Swiss Muon Source (SμS) and Swiss Light Source (SLS), Paul Scherrer Institute, Villigen, Switzerland. J.A.K. acknowledges support by the Swiss National Science Foundation (SNF-Grants No. 200021_165910 and No. P500PT_203159). I.P.R. acknowledges support from the Ministry of Education and Science of the Russian Federation within State Task No. FSWM-2020-0033. E.V.C. acknowledges funding by Saint Petersburg State University project for scientific investigations (ID No. 94031444). The work at the University of Warwick was supported by EPSRC, UK, through Grants No. EP/M028771/1 and No. EP/T005963/1. The magnetization measurements were supported by the Swiss National Science Foundation (SNF-Grant No. 206021_139082). N.B.M.S. was supported by Microsoft. We are grateful to C. W. Schneider for help with single crystal XRD measurements. We thank A. Doll, Z. Guguchia, and S. Holenstein from PSI,

Switzerland, and A. Chatzichristos, D. Fujimoto, V. L. Karner, R. M. L. McFadden, J. O. Ticknor, W. A. MacFarlane, and R. F. Kiefl from the University of British Columbia, Canada, for helpful discussions. Further, we note that a preliminary version of these results was published as part of a Ph.D. thesis [52].

[1] A. K. Geim and I. V. Grigorieva, Nature (London) **499**, 419 (2013).
[2] C. R. Rajamathi, U. Gupta, N. Kumar, H. Yang, Y. Sun, V. Süß, C. Shekhar, M. Schmidt, H. Blumtritt, P. Werner *et al.*, Adv. Mater. **29**, 1606202 (2017).
[3] R. Clarke, E. Marseglia, and H. P. Hughes, Philos. Mag. B **38**, 121 (1978).
[4] Y. Sun, S.-C. Wu, M. N. Ali, C. Felser, and B. Yan, Phys. Rev. B **92**, 161107(R) (2015).
[5] Y. Qi, P. G. Naumov, M. N. Ali, C. R. Rajamathi, W. Schnelle, O. Barkalov, M. Hanfland, S.-C. Wu, C. Shekhar, Y. Sun *et al.*, Nat. Commun. **7**, 11038 (2016).
[6] N. Xu, Z. W. Wang, A. Magrez, P. Bugnon, H. Berger, C. E. Matt, V. N. Strocov, N. C. Plumb, M. Radovic, E. Pomjakushina *et al.*, Phys. Rev. Lett. **121**, 136401 (2018).
[7] I. G. Lezama, A. Ubaldini, M. Longobardi, E. Giannini, C. Renner, A. B. Kuzmenko, and A. F. Morpurgo, 2D Mater. **1**, 021002 (2014).
[8] H. Xu, S. Fathipour, E. W. Kinder, A. C. Seabaugh, and S. K. Fullerton-Shirey, ACS Nano **9**, 4900 (2015).
[9] Y. Ding, N. Zhou, L. Gan, X. Yan, R. Wu, I. H. Abidi, A. Waleed, J. Pan, X. Ou, Q. Zhang *et al.*, Nano Energy **49**, 200 (2018).
[10] S. Song, D. H. Keum, S. Cho, D. Perello, Y. Kim, and Y. H. Lee, Nano Lett. **16**, 188 (2016).
[11] Y. Wang, J. Xiao, H. Zhu, Y. Li, Y. Alsaid, K. Y. Fong, Y. Zhou, S. Wang, W. Shi, Y. Wang *et al.*, Nature (London) **550**, 487 (2017).
[12] P. M. Coelho, H.-P. Komsa, K. Lasek, V. Kalappattil, J. Karthikeyan, M.-H. Phan, A. V. Krasheninnikov, and M. Batzill, Adv. Electron. Mater. **5**, 1900044 (2019).
[13] Z. Guguchia, A. Kerelsky, D. Edelberg, S. Banerjee, F. v. Rohr, D. Scullion, M. Augustin, M. Scully, D. A. Rhodes, Z. Shermadini *et al.*, Sci. Adv. **4**, eaat3672 (2018).
[14] Y. Ma, Y. Dai, M. Guo, C. Niu, J. Lu, and B. Huang, Phys. Chem. Chem. Phys. **13**, 15546 (2011).
[15] M. B. Kanoun, J. Alloys Compd. **748**, 938 (2018).
[16] F. R. Foronda, F. Lang, J. S. Möller, T. Lancaster, A. T. Boothroyd, F. L. Pratt, S. R. Giblin, D. Prabhakaran, and S. J. Blundell, Phys. Rev. Lett. **114**, 017602 (2015).
[17] T. Lancaster, S. J. Blundell, P. J. Baker, M. L. Brooks, W. Hayes, F. L. Pratt, J. L. Manson, M. M. Conner, and J. A. Schlueter, Phys. Rev. Lett. **99**, 267601 (2007).
[18] J. M. Wilkinson and S. J. Blundell, Phys. Rev. Lett. **125**, 087201 (2020).
[19] See Supplemental Material at http://link.aps.org/supplemental/10.1103/PhysRevMaterials.7.044414 for additional details about sample characterization (x ray photoemission core levels, x ray diffraction, stoichiometry and magnetization), ARPES measurements (k_z-conversion, calibration of charging effects and sample degradation), muon sites (coordinates, energies, and local spin densities), angular dependence of zero field μ^+SR, low-energy μ^+SR in the near-surface region, and temperature dependence of the ^{125}Te-NMR powder line shape and of the spin lattice relaxation rate, which also contains Refs. [13,14,23,27,29,45,53–56].
[20] E. Morenzoni, H. Glückler, T. Prokscha, H. P. Weber, E. M. Forgan, T. J. Jackson, H. Luetkens, C. Niedermayer, M. Pleines, M. Birke *et al.*, Phys. B: Condens. Matter **289-290**, 653 (2000).
[21] T. Prokscha, E. Morenzoni, K. Deiters, F. Foroughi, D. George, R. Kobler, A. Suter, and V. Vrankovic, Nucl. Instrum. Methods Phys. Res. A **595**, 317 (2008).
[22] A. Amato, H. Luetkens, K. Sedlak, A. Stoykov, R. Scheuermann, M. Elender, A. Raselli, and D. Graf, Rev. Sci. Instrum. **88**, 093301 (2017).
[23] A. Yaouanc and P. de Réotier, *Muon Spin Rotation, Relaxation, and Resonance: Applications to Condensed Matter*, International Series of Monographs on Physics (Oxford University Press, Oxford, 2011).
[24] A. Suter and B. M. Wojek, Phys. Procedia **30**, 69 (2012).
[25] R. K. Harris, E. D. Becker, S. M. C. d. Menezes, R. Goodfellow, and P. Granger, Magn. Reson. Chem. **40**, 489 (2002).
[26] V. N. Strocov, T. Schmitt, U. Flechsig, T. Schmidt, A. Imhof, Q. Chen, J. Raabe, R. Betemps, D. Zimoch, J. Krempasky *et al.*, J. Synchrotron Radiat. **17**, 631 (2010).
[27] V. N. Strocov, X. Wang, M. Shi, M. Kobayashi, J. Krempasky, C. Hess, T. Schmitt, and L. Patthey, J. Synchrotron Radiat. **21**, 32 (2014).
[28] V. N. Strocov, M. Shi, M. Kobayashi, C. Monney, X. Wang, J. Krempasky, T. Schmitt, L. Patthey, H. Berger, and P. Blaha, Phys. Rev. Lett. **109**, 086401 (2012).
[29] T. Böker, R. Severin, A. Müller, C. Janowitz, R. Manzke, D. Voß, P. Krüger, A. Mazur, and J. Pollmann, Phys. Rev. B **64**, 235305 (2001).
[30] G. Kresse and J. Furthmüller, Phys. Rev. B **54**, 11169 (1996).
[31] G. Kresse and D. Joubert, Phys. Rev. B **59**, 1758 (1999).
[32] J. P. Perdew, K. Burke, and M. Ernzerhof, Phys. Rev. Lett. **77**, 3865 (1996).
[33] J. S. Möller, D. Ceresoli, T. Lancaster, N. Marzari, and S. J. Blundell, Phys. Rev. B **87**, 121108(R) (2013).
[34] F. Bernardini, P. Bonfà, S. Massidda, and R. De Renzi, Phys. Rev. B **87**, 115148 (2013).
[35] G. Henkelman and H. Jónsson, J. Chem. Phys. **113**, 9978 (2000).
[36] T. Ozaki, Phys. Rev. B **67**, 155108 (2003).
[37] K. Momma and F. Izumi, J. Appl. Crystallogr. **44**, 1272 (2011).
[38] J. I. Budnick, L. J. Bruner, R. J. Blume, and E. L. Boyd, J. Appl. Phys. **32**, S120 (1961).
[39] D. Tay, T. Shang, P. Puphal, E. Pomjakushina, H.-R. Ott, and T. Shiroka, Phys. Rev. B **102**, 241109(R) (2020).
[40] Z. T. Zhang, D. Dmytriieva, S. Molatta, J. Wosnitza, Y. Wang, M. Helm, S. Zhou, and H. Kühne, Phys. Rev. B **95**, 085203 (2017).
[41] J. Perez-Mato, S. Gallego, E. Tasci, L. Elcoro, G. de la Flor, and M. Aroyo, Annu. Rev. Mater. Res. **45**, 217 (2015).

[42] F. Weber, R. Hott, R. Heid, L. L. Lev, M. Caputo, T. Schmitt, and V. N. Strocov, Phys. Rev. B **97**, 235122 (2018).
[43] D. Rhodes, R. Schönemann, N. Aryal, Q. Zhou, Q. R. Zhang, E. Kampert, Y.-C. Chiu, Y. Lai, Y. Shimura, G. T. McCandless *et al.*, Phys. Rev. B **96**, 165134 (2017).
[44] N. Aryal and E. Manousakis, Phys. Rev. B **99**, 035123 (2019).
[45] H. González-Herrero, J. M. Gómez-Rodríguez, P. Mallet, M. Moaied, J. J. Palacios, C. Salgado, M. M. Ugeda, J.-Y. Veuillen, F. Yndurain, and I. Brihuega, Science **352**, 437 (2016).
[46] B. D. Patterson, Rev. Mod. Phys. **60**, 69 (1988).
[47] S. F. J. Cox, J. Phys.: Condens. Matter **15**, R1727 (2003).
[48] M. Senba, Phys. Rev. A **62**, 042505 (2000).
[49] V. Baltz, A. Manchon, M. Tsoi, T. Moriyama, T. Ono, and Y. Tserkovnyak, Rev. Mod. Phys. **90**, 015005 (2018).
[50] J. D. Sau, S. Tewari, R. M. Lutchyn, T. D. Stanescu, and S. Das Sarma, Phys. Rev. B **82**, 214509 (2010).
[51] T. Hesjedal and Y. Chen, Nat. Mater. **16**, 3 (2017).
[52] J. A. Krieger, Doping and interface effects in topological materials, Ph.D. thesis, ETH Zurich, 2020, https://dx.doi.org/10.3929/ethz-b-000460760.
[53] S. Tongay, S. S. Varnoosfaderani, B. R. Appleton, J. Wu, and A. F. Hebard, Appl. Phys. Lett. **101**, 123105 (2012).
[54] M. Herak, A. Zorko, M. Pregelj, O. Zaharko, G. Posnjak, Z. Jagličić, A. Potočnik, H. Luetkens, J. van Tol, A. Ozarowski *et al.*, Phys. Rev. B **87**, 104413 (2013).
[55] Y. Tian, N. Ghassemi, and J. H. Ross, Phys. Rev. B **102**, 165149 (2020).
[56] Y. Tian, Y. Zhu, R. Li, Z. Mao, and J. H. Ross, Phys. Rev. B **104**, L041105 (2021).